Earth and Planetary Science Letters 281 (2009) 88–98

Contents lists available at ScienceDirect

Earth and Planetary Science Letters

journal homepage: www.elsevier.com/locate/epsl

Leucite crystals: Surviving witnesses of magmatic processes preceding the 79AD eruption at Vesuvius, Italy

Thomas Shea [a,*], Jessica F. Larsen [b], Lucia Gurioli [a], Julia E. Hammer [a], Bruce F. Houghton [a], Raffaello Cioni [c]

[a] *Department of Geology and Geophysics, SOEST, University of Hawaii, 96822, Honolulu, HI, United States*
[b] *Geophysical Institute, University of Alaska Fairbanks, 99775, Fairbanks, AK, United States*
[c] *Dip. Scienze della Terra, Università degli Studi di Cagliari, 01927, Cagliari, Italy*

ARTICLE INFO

Article history:
Received 1 September 2008
Received in revised form 7 February 2009
Accepted 9 February 2009
Available online 18 March 2009

Editor: R.W. Carlson

Keywords:
leucite
phonolite
Vesuvius
decompression experiments
magma chamber
crystallization kinetics

ABSTRACT

Crystals in volcanic rocks are sensitive records of magma chamber and conduit conditions under volcanoes. Plagioclase is an invaluable tool to identify ascent rates for calc-alkaline magmas, but may be absent in alkaline melts. In contrast, leucite is common in alkaline magmas and is potentially useful to investigate storage and ascent conditions prior to volcanic eruptions. Leucite microphenocrysts are ubiquitous within the products from all phases of the 79AD eruption of Vesuvius. Steady-state (isobaric–isothermal) and dynamic (decompression) experiments on white phonolitic pumice from the opening (EU1) and lower Plinian (EU2) phases of the eruption were performed at temperature conditions ranging from 800 to 850 °C to test the possibility that leucites within this 'white' magma formed during ascent. However, multiple-step decompression (MSD) experiments using a decompression rate of 0.25 MPa/s failed to crystallize leucite even at pressures well below its stability domain. On the other hand, single-step decompression (SSD) experiments from 150 MPa to 25 MPa result in leucite crystallization after a ~12 h lag period, but the skeletal habit and size distribution differ from those seen in natural pumices. Instead, euhedral leucites texturally matching those observed in 79 AD samples formed after 5 days under isobaric and isothermal (IB–IT) experimental conditions. Crystallization conditions derived from the latter experiments suggest the magma reservoir was thermally zoned with cooler EU1 ($T = 830$–840 °C) overlying slightly hotter EU2 ($T = 850$–925 °C) magma. Two models for natural crystallization conditions are consistent with the experimental data: either leucites formed at ~4 km depth ($P \sim 100$ MPa) in a steady storage environment inside a magma saturated with H_2O-rich vapor, or, alternatively, the white magma was initially undersaturated with respect to H_2O and leucites formed during a slow depressurization event prior to the eruption. Leucite crystallization seemingly adheres to the classical nucleation theory, and supports a compositional (i.e. H_2O) control on surface tension. Derived leucite growth rates reach $\sim 10^{-7}$ mm s^{-1} minimum, comparable to the fastest growth rates observed for plagioclase crystals in calc-alkaline magmas.

Published by Elsevier B.V.

1. Introduction

Vesuvius, Italy, entered the history of volcanology via Pliny the Younger, who documented the famous eruption that devastated the Roman towns of Herculaneum, Pompeii, Stabiae and Oplontis in 79AD (e.g. Sigurdsson et al., 1985). Because the volcano's flanks now have a population exceeding 500,000, it is a key focus of volcanology research. Despite being very well studied, the pre and syn-eruptive magmatic processes related to the 79 AD event are complex, and still poorly understood. This eruption emitted 2–2.8 km^3 DRE (dense rock equivalent) magma in less than 30 h as a complex succession of fall and pyroclastic density currents (PDC's), e.g. Lirer et al. (1973), Sheridan et al. (1981), Sigurdsson et al. (1985), designated EU1–8 from base to top (Cioni et al., 1992). During the eruption, magma composition shifted sequentially from "white" K-phonolite to "gray" K-tephriphonolite (e.g. Carey and Sigurdsson, 1987; Cioni et al., 1995). The phonolitic end-member possibly represents residual tephriphonolitic magma from the Avellino eruption (~3900 years BP), which subsequently fractionated to form the upper, compositionally layered portion of the 79 AD magma chamber (Cioni et al., 1995). In contrast, the "gray" tephriphonolite erupted in 79 AD is a mixture of more mafic, K-tephritic magma, periodically injected into the chamber, with the pre-existing K-phonolitic magma (e.g. Cioni et al., 1995).

The early erupted white magma deposits are divided into EU1 and EU2 fall layers, separated by proximal, locally dispersed PDC deposits. Chemically, EU1 and EU2 bulk compositions show only minor variations in their major elements, with SiO_2, MgO, CaO being slightly higher in EU2 and Na_2O, Al_2O_3 and K_2O being somewhat higher in EU1 (Table 1). EU1 and EU2 pumices both have a complex mineralogy, with phenocrysts of alkali feldspar, clinopyroxene, amphibole, mica, garnet, and minor plagioclase and Fe–Ti oxides, in order of decreasing

---

[*] Corresponding author. Tel.: +1 808 956 8558.
E-mail address: tshea@hawaii.edu (T. Shea).

0012-821X/$ – see front matter. Published by Elsevier B.V.
doi:10.1016/j.epsl.2009.02.014

Table 1
Major element chemistry for EU1 and EU2 natural samples.

wt. %	EU1 14-1	EU2 V15-2-9
SiO_2	54.91 (0.26)	55.41 (0.38)
TiO_2	0.31 (0.14)	0.26 (0.11)
Al_2O_3	22.30 (0.23)	21.97 (0.45)
FeO*	2.16 (0.13)	2.90 (0.38)
MnO	0.24 (0.08)	0.24 (0.12)
MgO	0.23 (0.03)	0.65 (0.07)
CaO	3.11 (0.22)	3.69 (0.25)
Na_2O	6.22 (0.19)	5.32 (0.21)
K_2O	9.89 (0.42)	9.17 (0.39)
Cl[a]	0.54 (0.08)	0.26 (0.14)
P_2O_5	0.09 (0.04)	0.12 (0.05)
Totals[b]	99.20 (0.41)	99.76 (0.58)
n[c]	14	19

[a] Cl is reported as oxide weight percent.
[b] Original totals with analyses normalized to 100%.
[c] Total number of electron microprobe analyses of glass created by melting powders in $Au_{75}Pd_{25}$ tubing for 10 min at 1300 °C.

volumetric abundance, enclosed in a glassy groundmass with microphenocrysts/microlites of leucite, sanidine, pyroxene and amphibole (Cioni et al., 1995). Although less abundant volumetrically than sanidine, leucites are more numerous in the 79 AD pumice samples and typically measure 25 µm in diameter (Gurioli et al., 2005). In general, crystal size is intrinsically linked to nucleation and growth conditions (Cashman, 1992), with phenocrysts (>100 µm) usually formed within a magma reservoir, and microlites (<30 µm) growing during ascent or cooling after extrusion. The 25 µm size of the 79 AD leucites falls between microlites and microphenocrysts, a size range for which conditions of formation are equivocal. Here, we examine whether the 79 AD Vesuvius leucite crystallized during rapid magma ascent akin to plagioclase microlites in other magmatic systems (e.g. Cashman, 1992; Geschwind and Rutherford, 1995), or whether they formed at low degrees of undercooling in a more “static” storage environment prior to eruption.

2. Methods

2.1. Phase stability

The use of phase equilibria experiments to investigate the stability of crystals in a given magma is aided by independent knowledge of the major volatile contents and fO_2 conditions. Water saturation (i.e. $X^{fl}_{H2O} \approx 1$) was found by Rutherford (1996) to be consistent with the crystallization of the mineral assemblage present in the 79 AD phonolite. The absence of measurable CO_2 in melt-inclusions, also supports water saturation conditions, and was interpreted to result from CO_2-degassing at magma chamber depth (Cioni, 2000). Even if the magma was CO_2-poor immediately prior to eruption, it may have been present in the melt at an earlier stage of magmatic evolution (Scaillet and Pichavant, 2004).

All experiments employed H_2O-saturated conditions and fO_2 was maintained at Ni–NiO + 0.5 to 1 log unit (Rutherford, 1996; Scaillet and Pichavant, 2004) by inserting Ni-filler rods in Waspaloy pressure vessels. The starting materials consisted of finely powdered EU1 and EU2 natural pumice, welded inside $Ag_{70}Pd_{30}$ or Au capsules with ~10% de-ionized H_2O to ensure saturation. The experiments were run at $T = 800–1000$ °C and $P_{H2O} = 25–200$ MPa for 5–9 days (Table 2), and quenched in water. Mineral stability for all detected phases was assessed by inspection of crystal morphology and reaction/dissolution textures using Scanning Electron Microscopy (SEM) and EDS analysis, in order to construct phase diagrams for both EU1 and EU2 (Fig. 1). Reversals (R4 to R11 in Table 2), were performed at chosen P–T conditions to refine the location of the leucite-in curves.

2.2. Single and multiple-step decompression experiments

The decompression experiments were run using two approaches. Single-step decompressions were achieved through rapid decompression to 25 MPa, and holding for 5 min to 7 days before quenching, replicating integrated decompression rates of 0.0002 to 0.41 MPa s^{-1} (Table A1 in data repository). Through this method, we aimed to characterize the evolution of nucleation and growth rate following a large thermodynamic perturbation (Hammer and Rutherford, 2002).

Table 2
Phase equilibria and reversal experimental conditions, with performed leucite measurements.

Sample name	Type-series	P (MPa)	T (°C)	*t* (hours) at P	Lc
Phase Eq.					
EU1					
79ADEU1–2	Phase Eq	150	850	152	no
79ADEU1–3	Phase Eq	150	800	163	no
79ADEU1-4	Phase Eq	150	850	163	no
79ADEU1-5	Phase Eq	100	825	212	yes
79ADEU1-6	Phase Eq	150	825	212	no
79ADEU1-7	Phase Eq	50	825	212	yes
79ADEU1-8	Phase Eq	50	850	212	yes
79ADEU1-10	Phase Eq	100	875	164	yes
79ADEU1-11	Phase Eq	100	850	164	yes
79ADEU1-12	Phase Eq	200	850	164	no
79ADEU1-13	Phase Eq	100	840	188	yes
79ADEU1-14	Phase Eq	150	840	188	no
79ADEU1-16	Phase Eq	175	825	166	no
79ADEU1-17	Phase Eq	100	810	166	no
79ADEU1-18	Phase Eq	50	800	166	yes
EU2					
79ADEU2-1	Phase Eq	150	850	162	no
79ADEU2-2	Phase Eq	150	800	163	no
79ADEU2-3	Phase Eq	150	850	188	no
79ADEU2-5	Phase Eq	125	830	120	no
79ADEU2-7	Phase Eq	50	840	125	yes
79ADEU2-8	Phase Eq	150	800	125	no
79ADEU2-9	Phase Eq	50	800	120	yes
79ADEU2-10	Phase Eq	150	825	122	no
79ADEU2-11	Phase Eq	100	850	144	no
79ADEU2-12	Phase Eq	150	850	137	no
79ADEU2-14	Phase Eq	200	815	168	no
79ADEU2-15	Phase Eq	200	850	144	no
79V1	Phase Eq	75	880	72	yes
79V2	Phase Eq	150	850	144	no
79V3	Phase Eq	150	880	23	no
79VB21	Phase Eq	200	800	23	no
79VB22	Phase Eq	200	840	24	no
79VB24	Phase Eq	100	800	24	yes
79VS10	Phase Eq	50	880	28	yes
Reversals					
EU1					
R4-EU1-10	Reversal	25	880	156	yes
R4-EU1-8	Reversal	25	880	156	yes
R5-EU1-13	Reversal	175	800	144	no
R5-EU1-16	Reversal	175	800	144	no
R6-EU1-5	Reversal	125	825	120	yes
R6-EU1-6	Reversal	125	825	120	yes
R7-EU1-13	Reversal	115	840	120	yes
R7-EU1-14	Reversal	115	840	120	yes
R8-EU1-18	Reversal	125	800	120	no
R8-EU1-13	Reversal	125	800	120	no
EU2					
R4-EU2-7	Reversal	25	880	156	yes
R4-EU2-79VB7	Reversal	25	880	156	yes
R5-EU2-5	Reversal	175	800	144	no
R5-EU2-79VB21	Reversal	175	800	144	no
R9-EU2-7	Reversal	100	840	120	yes
R9-EU2-5	Reversal	100	840	120	yes
R10-EU2-5	Reversal	80	860	132	yes
R10-EU2-79V1	Reversal	80	860	132	yes
R11-EU2-79VB21	Reversal	125	800	144	no
R11-EU2-9	Reversal	125	800	144	no

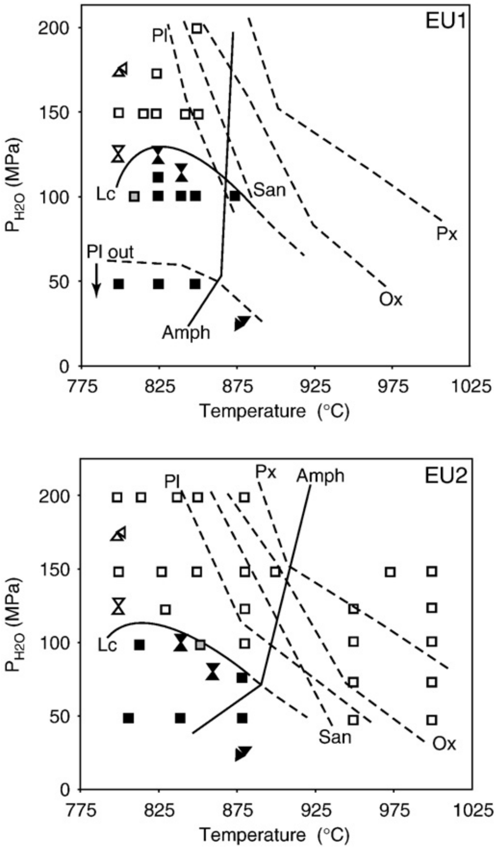

Fig. 1. Phase diagram derived from IB–IT experiments, which will be described in more detail in a separate study that will focus on crystallization of all phases in the 79 AD phonolites. Stability curves in P_{H2O}–T space for (a) EU1 and (b) EU2; empty symbols represent leucite-free experiments, and black symbols experiments in which leucite crystallized. Double triangles symbolize reversal experiments, used to fine-tune stability curves. For most reversals, leucite stability was approached from both sides of the curve (i.e. crystallization and melting). As mentioned in the text, EU1 and EU2 also crystallized garnet and mica, however, their position in the P–T space is not well constrained by the experiments we currently possess.

Multiple-step decompression experiments were run with 5 MPa pressure drops followed by 20-second hold times after each step, simulating a linear decompression rate of 0.25 MPa/s (Table A2). This rate was chosen to replicate a 10 m/s average magma ascent rate, calculated after models from Papale and Dobran (1993). This value is well within the range determined for explosive Plinian eruptions (0.1 to 20 m/s, Gardner et al., 1999; 2000; Rutherford and Gardner, 2000) and is conservative compared to the 30–40 m/s ascent rates required to reproduce discharge rates calculated for the 79 AD eruption (CONFLOW, Mastin, 2002). Although magmatic ascent in nature is probably non-linear, use of a linear decompression rate of 0.25 MPa/s is considered an acceptable approximation given a short total magma ascent timescale of several minutes. In both cases, the experiments were conducted using run products equilibrated previously for 5–7 days at pressure conditions above the stability curve (150 MPa or 200 MPa) to obtain leucite-free starting materials (Fig. 1). The experimental temperatures of 800–850 °C encompass a range determined for the 79 AD magmas from prior studies (Barberi et al., 1981; Cioni et al., 1995).

3. Results

The position of the leucite stability curves in both EU1 and EU2 bulk compositions are reported in Fig. 1. The dashed curves show the approximate stabilities of major phases crystallized: plagioclase, oxides, sanidine, and pyroxene. The amphibole curves are shown by solid lines to emphasize their wide stability ranges in both EU1 and EU2 at the experimental conditions. The leucite stability curves are relatively constant in pressure, ranging between ~75 and 125 MPa in both EU1 and EU2 compositions at temperatures up to at least 880 °C. The higher temperature experiments in EU2 show no leucites at $T = 950$ °C and P_{H2O} as low as 50 MPa.

3.1. Leucite morphology in decompression experiments

In the natural pumices, leucites are clean, unzoned, euhedral crystals homogeneously distributed within glass (Fig. 2a and b). In contrast, the EU1 and EU2 SSD experiments produced skeletal leucites (see additional material, Fig. A1), that grew into branching clusters, irrespective of hold time and temperature. With increasing time at the final pressure (5 to 10,080 min at 25 MPa), leucite shapes successively varied from small skeletal clusters to dendritic branches to massive, formless leucite domains (Fig. A1, Table A1). These complex habits and the heterogeneous distribution of leucites in EU1 and EU2 SSD are far different from those observed in the natural samples. Although the MSD series were run to approximate the average ascent rate of the 79 AD magma, none of the MSD experiments crystallized leucites, even at 25 MPa, which is well within the leucite stability field (Fig. 1). Simple textural observations from both SSD and MSD experiments show that neither decompression series replicated leucite formation in the natural magmas.

3.2. Isothermal–isobaric experiments applied to leucite formation in the 79 AD magmas

Because the decompression experiments did not yield leucites that compare well with those enclosed by 79 AD white pumices, we examined the leucites that formed in the phase equilibria experiments since their textural characteristics match very well those observed in nature. In essence, the phase equilibria experiments better approximate to low degrees of undercooling and crystallization at near-equilibrium conditions, more appropriate for a magma reservoir than a conduit. The phase equilibria experiments are labeled isothermal and isobaric (IB–IT) experiments hereafter, to draw a clear distinction with the rapid changes induced during decompression. Similarly, reversal experiments provided verification of the leucite stability curves, as well as validation of the IB–IT experiments to characterize leucite textures. If the textures of the reversal experiments are similar whether approached via melting or crystallization from either side of the curve, then the observed textures do not depend on prior equilibration conditions.

3.2.1. Leucite morphology in IB–IT experiments

In general, natural textures were reproduced in IB–IT runs (Fig. 2c and d), with some apparent variations between EU1 and EU2 experiments. Nearly all EU1 runs produced equant, homogeneously distributed leucites. The only exception to this is experiment 79ADEU1–18, run at relatively low pressure and temperature ($T = 800$ °C, $P = 50$ MPa), in which clusters of leucites were observed instead of free crystals. Most EU2 leucites in runs below 850 °C strongly cluster around small vesicles (Fig. 2f), while above 850 °C, the EU2 leucites are spatially homogeneous and equant, akin to those formed in EU1 at $T > 800$ °C. Hence, at $T = 800$ °C in EU1, and at $T < 850$ °C in EU2, IB–IT-derived leucites are texturally comparable to those formed in SSD experiments. Only above these temperatures do leucites grow similarly to their natural counterparts. Lastly, close to the inferred leucite stability boundary, EU1 experiments crystallized only a few very large individual crystals (Fig. 2e).

3.2.2. Leucite textural characterization

In using the IB–IT experiments to draw kinetic information, we assume that the mechanically as well as thermodynamically

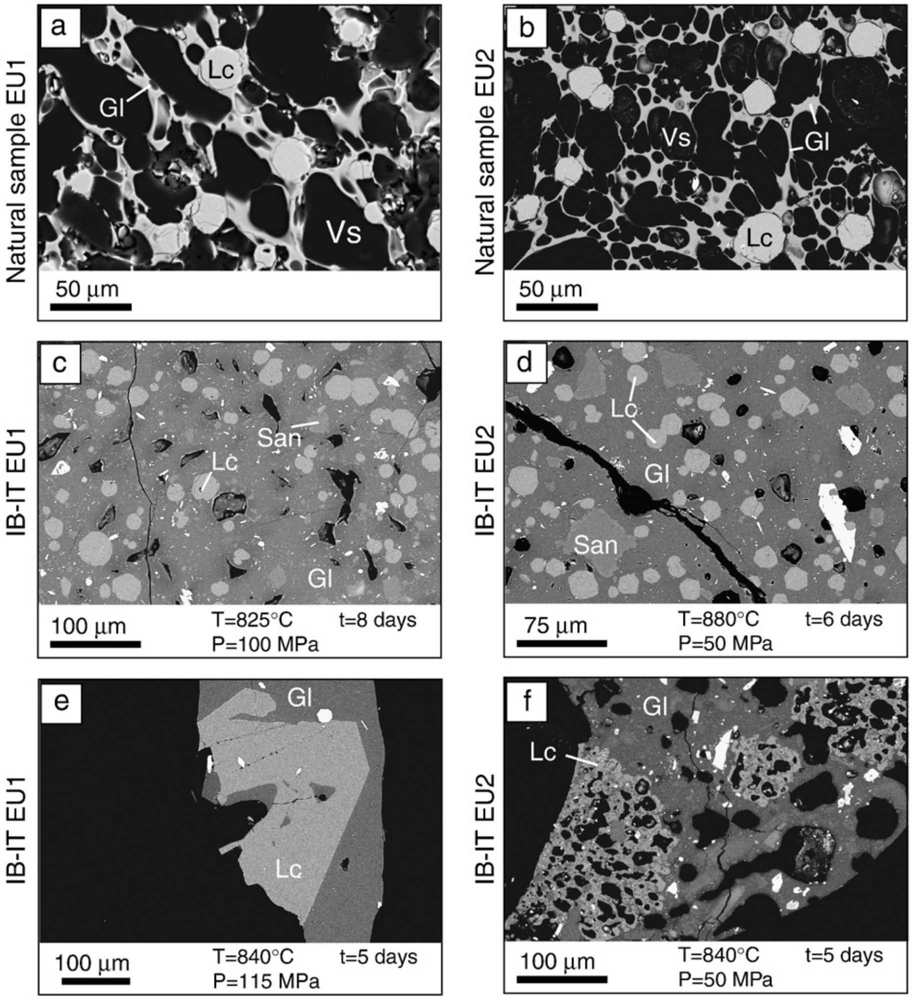

Fig. 2. BSEM images of selected samples. (a) and (b) EU1 and EU2 natural samples, highly vesicular containing euhedral, homogeneously distributed leucites. (c) and (d) EU1 and EU2 IB–IT runs respectively. (e) Typical growth texture of a very large EU1 leucite which crystallized very close to the phase's stability curve. Growth of this crystal was likely to have been limited by available space. (f) EU2 phase equilibria leucites formed at temperatures below $T=850$ °C are skeletal and clustered. Lc = leucite, Kfs = K-feldspar, Gl = Glass, Vesicles/pore spaces in black in the SEM images.

perturbed experimental system will return to chemical and textural equilibrium at the new P–T conditions. The time interval used to derive crystallization rates then becomes the time necessary to reach equilibrium. Taking into account that pulverizing the starting material in which leucites are present might have a strong influence on the experimental crystal number densities (N_V's) and derived nucleation rates, a section addresses these matters in the discussion.

Experimental and natural crystal content (vol.%), number density (N_V), and size (mean, maximum and mean of 5 largest crystals in μm), are used to derive average and maximum leucite nucleation rates I (mm^{-3} s^{-1}) and growth rates Y (mm s^{-1}) (Table 3), using the 5-day run duration that was inferred to ensure near-equilibrium conditions. Experiments which were run longer (8–9 days) do not show substantial mean size differences (e.g. 79ADEU1–5). Thus, the 5 day-period is preferred over longer run times and probably represents a maximum since equilibrium conditions may have been reached earlier. The quantification task proved much more difficult for EU2 than for EU1 because half of the charges containing leucites lacked discrete crystals appropriate for size measurements (e.g. Fig. 2f).

In both EU1 and EU2, the leucite stability field is confined to pressures below ~125 MPa at a relatively wide range in temperatures. N_V, and mean sizes d_{mean}, are used to calculate the time-averaged nucleation and growth rates versus pressure in Fig. 3. Although few data are available for EU2, the estimated nucleation rates I for EU1 and EU2 are indistinguishable as a function of experimental pressure below the stability limit at 125 MPa, and increase exponentially from ~10^{-3} $mm^{-3}s^{-1}$ at ~125 MPa, to 0.34 $mm^{-3}s^{-1}$ at 25 MPa (Fig. 3).

In contrast, leucite growth rates are highest close to the upper stability pressure (~125 MPa), with EU1 growth rates exceeding 4×10^{-8} mm s^{-1} for the three experiments closest to 125 MPa, decaying to $2\text{–}3\times10^{-8}$ mm s^{-1} at ~100 MPa, and remaining nearly constant at lower pressures. Two fits of comparable R^2~0.90 values are proposed: in Data Fit A (Fig. 3), growth rates attain their peak on the stability limit, and, alternatively, in Data Fit B, growth rates reach a maximum shortly before the stability pressure conditions. In both cases, the offset between nucleation and growth rate curves with respect to effective undercooling are consistent with previous work and the classical theory (Kirkpatrick, 1981; Hammer and Rutherford, 2002; Couch et al., 2003). With the exception of the EU1 experiments run very close to the leucite stability curve (EU1–10, R6EU1–6, R7EU1–13, see Fig. 1), mean size does not vary significantly throughout the P–T domain examined. Although fewer data exists for EU2, those experiments also show consistent behavior with a shift towards lower sizes compared to EU1 (Data Fit C).

The relatively constant average growth rates and sizes observed in both EU1 and EU2 experiments allows us to merge the CSDs, obtained from static experiments, into two size distribution plots shown in Fig. 4 (also see Table 3). We excluded the EU1 experiments EU1–10, R6EU1–6 and R7EU1–13 because their growth rates are variable, and fewer than 15 crystals were observed. Typically, EU1 and EU2 leucites

Table 3
Leucite crystallization results from EU1 and EU2 experiments and natural pumices.

	P (MPa)	T (°C)	*n* (#)	[a]Lc%	[b]*d* mean (μm)	*d* mode (μm)	[c]*d* max (μm)	[c]*d* max$_5$ (μm)	[d]Y$_{mean}$ mm s^{-1} × 10^{-8}	[d]Y$_{max5}$ mm s^{-1} × 10^{-8}	[e]Nv mm^{-3} × 10^{-4}	[f]I mm^{-3} s^{-1}
Individual experimental results												
IB–IT												
79ADEU1-5	100	825	1468	12.5	24.0	25	65	53.7	2.78	6.21	3.18	0.074
79ADEU1-7	50	825	2045	23.0	22.6	25	74	62.7	2.61	7.26	7.94	0.184
79ADEU1-8	50	850	1842	21.0	24.4	25	82	70.1	2.83	8.11	6.13	0.142
79ADEU1-10	100	875	741	11.5	37.1	31.5	94	84.2	4.3	9.74	1.31	0.03
79ADEU1-11	100	850	1531	13.5	26.7	25	82	73.6	3.09	8.52	2.20	0.051
79ADEU1-13	100	840	1951	16.7	28.8	25	102	76	3.33	9.08	3.73	0.086
79V1	75	880	1002	14.1	17.7	16	43	38.7	2.06	4.48	3.85	0.089
79VS10	50	880	1219	18.8	16.4	20	40	35.9	1.9	4.15	5.36	0.124
Reversals												
R4-EU1-8	25	880	933	30.7	21.4	20	45	44	2.48	5.09	14.70	0.34
R6-EU1-6	125	825	46	nd	54.0	nd	65	nd	6.25	nd	0.22	0.005
R7-EU1-13	115	840	23	nd	70.0	nd	140	nd	8.1	nd	0.03	0.0007
R10-EU2-5	80	860	211	15.2	16.5	16	27	25.9	1.9	3	4.69	0.108
Grouped experimental results												
EU1 natural	–	–	1328	17.91	24.4 (5.8)	25	57.6	74	–	–	3.12	–
EU1 exp.	–	–	8458	16.55 (4.8)	25.8 (5.3)	25	77.3 (10.6)	102	2.98 (0.28)	8.95 (1.12)	4.03	0.093 (0.06)
EU2 natural	–	–	965	13.82	19.0 (6.2)	16–20	41.2	49	–	–	4.55	–
EU2 exp.	–	–	2221	16.06 (2.5)	19.6 (6.8)	16–20	33.8 (6.7)	43	1.95 (0.15)	3.91 (0.23)	5.63	0.107 (0.05)

n is number of crystals measured.

[a] Leucite volume %.

[b] Mean diameter (d_{mean}).

[c] Mean size of 5 largest crystals (d_{max5}) and size of largest crystals (d_{max}).

[d] Time-averaged, mean growth rates (Y_{mean}) and growth rates for 5 largest crystals (Y_{max}).

[e] Number of leucites per unit volume (N_V) corrected for vesicularity.

[f] Time-averaged nucleation rate (I) derived from N_V.

in both IB–IT and natural samples show very similar unimodal distributions. However, the leucite size distributions in the two compositions are distinctly different in terms of their sizes, volume fractions, and number densities.

EU1 experiments and natural pumices have indistinguishable mean sizes of $d_{mean} = 25.8 \pm 5.3$ μm and $d_{mean} = 24.4 \pm 5.8$ μm respectively (Table 3), slightly larger than those observed in EU2, in which mean sizes are $d_{mean} = 19.0 \pm 6.2$ μm in natural samples and $d_{mean} = 19.6 \pm 6.8$ μm in the experiments. For EU1 and EU2 experiments, calculated average growth rates are $Y_{mean} = 2.98 \times 10^{-8}$ mm s^{-1}, and $Y_{mean} = 1.95 \times 10^{-8}$ mm s^{-1} respectively. The mean sizes of the five largest EU1 leucites are 57.6 and 77.3 μm in experimental and natural samples respectively. Those are larger than their EU2 counterparts, with 33.8 and 41.2 μm respectively. Thus, average growth rates derived from the five largest EU1 experimental crystals are $Y_{max5} = 8.95 \times 10^{-8}$ mm s^{-1}, nearly twice as large as those calculated for EU2 ($Y_{max5} = 3.91 \times 10^{-8}$ mm s^{-1}). Both natural pumice and experimental leucite histograms from EU1 also possess a distinctive modal peak at equivalent diameters of 25 μm, while those from EU2 lack a clear mode. R6EU1–6 and R7EU1–13 contained the largest leucites of the experimental set ($d_{mean} = 54$ μm and $d_{mean} = 70$ μm respectively) and, consequently, yielded much higher mean growth rates ($Y_{mean} = 6.25 \times 10^{-8}$ mm s^{-1} and 8.1×10^{-8} mm s^{-1}).

While leucite size is relatively invariant as a function of experimental pressure (≤100 MPa; Fig. 3) or temperature, crystal volume fraction increases significantly as pressure decreases. At 100 MPa, leucites comprise 11.5–16.7 vol.%, corrected for vesicularity, while at 50 to 25 MPa, they make up 21–30.7 vol.% of EU1 experiments. Therefore, as pressure decreases and crystallization advances, size remains constant while leucite volume fraction doubles. This trend is clear in the case of EU1 but unconvincing in EU2, possibly reflecting the smaller range of experimental pressures that yielded individual, euhedral leucites.

Experimental leucites have somewhat higher number densities per unit volume than the natural samples, with $N_V \approx 4.03 \times 10^4$ mm^{-3} in EU1 and $N_V \approx 5.63 \times 10^4$ mm^{-3} in EU2. In contrast, the natural pumices have $N_V \approx 3.12 \times 10^4$ and 4.55×10^4 mm^{-3} for EU1 and EU2 respectively. This is clearly visible in a plot of ln(*n*) (*n* is number of leucites) versus crystal size (Fig. 5a), in which the experimental samples show a consistent shift towards higher number densities compared with the natural pumices, despite similarities in the overall shapes of the curves. This is most likely an effect caused by grouping the data; while leucite size is mostly invariant throughout EU1 and EU2 and justifies using an “integrated” size distribution, number densities vary substantially in between experiments and should be treated individually. When N_V is plotted against leucite volume % (Fig. 5b), the relationship becomes quite clear: leucite volume % increases with number density. The natural EU1 pumice leucite number density and volume fraction closely matches experiment EU1–13 ($P = 100$ MPa, $T = 840$ °C).

4. Discussion

4.1. Crystallization during decompression

Leucite habits in the SSD experiments are unusual compared with the natural leucites, indicating crystallization began in a nucleation dominant regime, followed by a period of rapid growth, as the crystals eventually merge and form large branched aggregates (see Fig. A1 in the additional material). Leucite nucleation in the SSD experiments occurred after an average of 1250 min at 25 MPa, indicating a substantial nucleation lag period hardly reconcilable with the ~8 min inferred for the magma to rise through the conduit (Papale and Dobran, 1993). Even the fastest-growing leucites formed only after 30 min (79ADEU1–6c, Table 3), which would imply a total ascent timescale four times slower than that postulated by Papale and Dobran (1993), and about ten times slower than that which is needed to produce the discharge rates calculated for this eruption. The complex SSD leucite shapes and the complete lack of leucites in MSD runs provide clear evidence that the decompression experiments do not replicate leucite

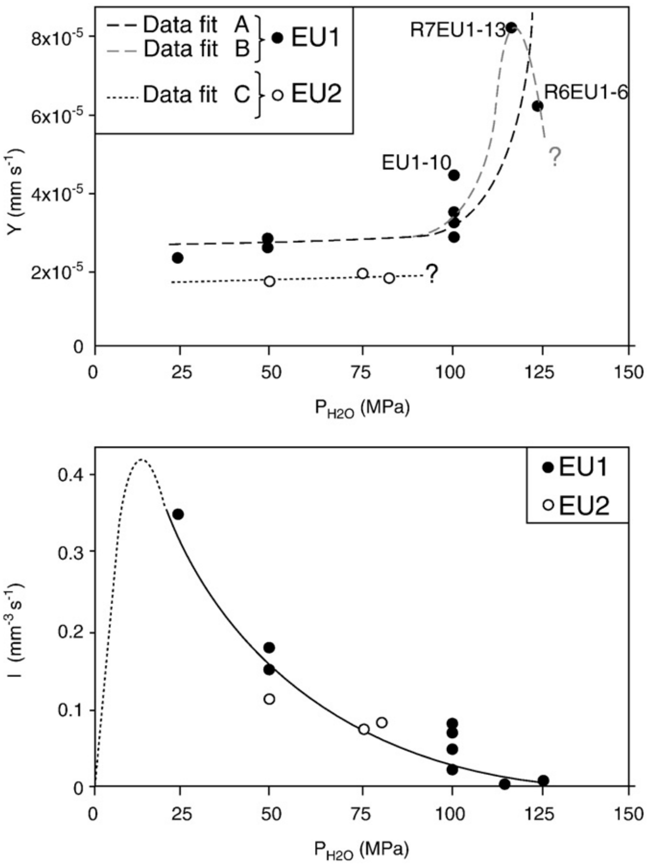

Fig. 3. The complex interplay between leucite growth and nucleation in EU1 and EU2. Around 100–125 MPa, close to the leucite-in boundary, nucleation rates are extremely low while growth rates are at their peak. As pressure decreases, growth rates stabilize while nucleation rates increase exponentially. The black dashed line (Data fit A) in the upper plot represents the scenario where growth rates peak at the phase boundary, and the grey dashed line (Data fit B) presents the case where growth rates are maximized slightly further from the stability curve. The few experiments available for EU2 show that differences might exist only in growth rates (i.e. dotted line “Data fit C” is shifted towards lower values). Black curve in centre of the plot shows a logarithmic fit of the form $I = -1.9325 \times 10^8 \ln(P) + 9.42 \times 10^8$ ($R^2 = 0.95$) between 25 and 125 MPa, which is later used to obtain surface tension from classic nucleation theory formulations.

formation in the 79 AD phonolite magmas. Probably low melt viscosity fosters a very fast ascent during Plinian eruptions, not allowing for leucite crystallization in the conduit. Instead, most water-saturated IB–IT experiments replicate the size ranges (15–25 µm) as well as the textural contrasts observed between EU1 and EU2 natural leucites, with EU2 containing smaller crystals on average than EU1. Most IB–IT experiments in which nature-like leucites form, were run at a lower degree of undercooling with respect to the leucite stability curve (Fig. 1). Moreover, the undercooling in the IB–IT runs is generally imposed over longer average timescales than in the decompression experiments. Hence, the crystal-melt system was able to respond and reach a near-equilibrium state only when the imposed experimental conditions were approximately isobaric and isothermal at relatively low degrees of undercooling.

4.2. Influence of initial material on experimentally-derived textures

The starting materials used for the experiments and how they are treated prior to experimentation may influence the outcome. For example, the use of natural crushed pumices could produce different results depending on whether the powders are first fused to very high temperature and then subjected to lower temperatures, or whether unmodified powdered natural material is used. To test whether the leucites formed in IB–IT experiments bear evidence for crystal textures inherited from the starting powders, we compare features of the experimental number densities, crystal shapes, and results from the reversal experiments with that expected given completely inherited textures from the starting materials.

To test the possibility that leucites grew from a melt initially depleted in crystalline phases, we conducted four IB–IT experiments at 100 MPa and 800 to 850 °C, for which the powders were first equilibrated at H_2O-saturation at 1000 °C and 100 MPa for 72 h. Those experiments were then quenched and splits of the material were re-loaded into new capsules in the presence of H_2O and run at 800 to 850 °C at 100 MPa for 90 to 120 h. The resulting experiments contained no recognizable minerals (79VB2, and 79VB9 to 13, Table 2). Instead, the melts appeared to segregate into domains that have compositions similar to sanidine or leucite (high K and high Al), but with non-stoichiometric oxide ratios. Thus, it appears that

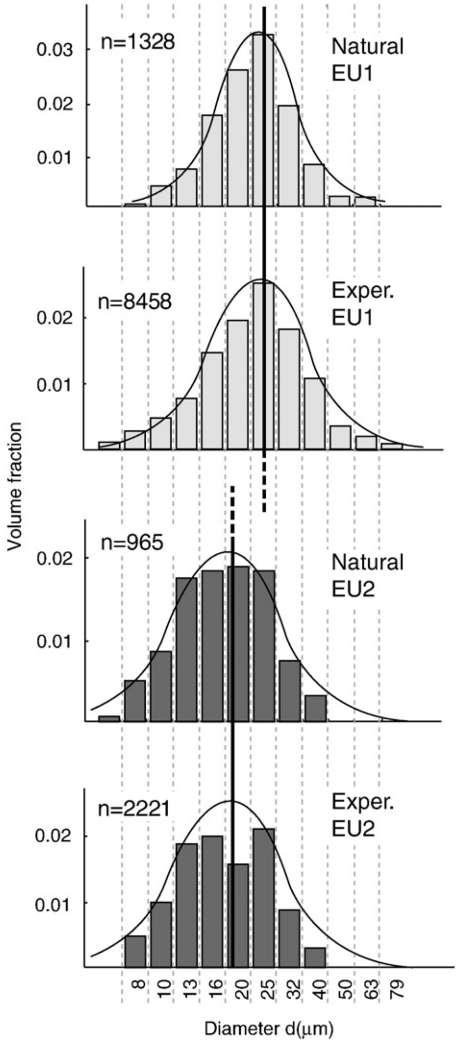

Fig. 4. Comparisons between leucites formed in static experiments and those observed in natural samples. Leucite size distribution in terms of volume for EU1/EU2 pumices and static experiments, are obtained using the stereological conversion method derived by Sahagian and Proussevitch (1998) and binned using geometric size classes. *N* is number of measured leucites.

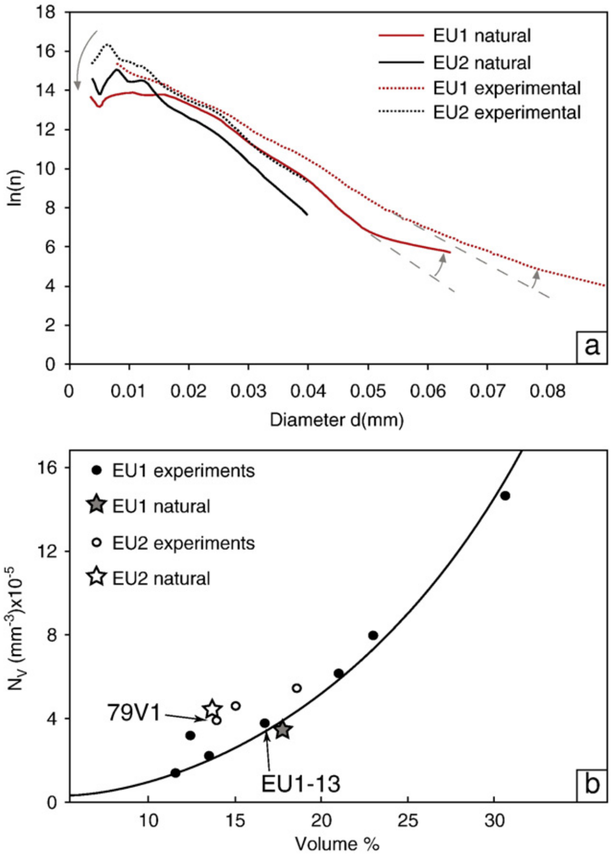

Fig. 5. (a) Leucite size distribution in terms of number. Note the good correspondence in terms of curve shape between experiments and natural samples. Also, note the systematic shift towards higher N_V in both cases, probably due to grouping of the experimental data. Grey arrows illustrate the possibility of coarsening processes affecting the distribution by reducing small individuals to increase larger ones. (b) Plot of leucite number density N_V against volume fraction. The clear relationship indicates leucite content increases in volume by nucleation rather than by growth. Natural samples are also placed for comparison.

the super-liquidus pre-annealing step disturbed the melt structure to the point where the activation energy barriers for crystal nucleation were not overcome during the experimental time-frame. Most likely, this process eliminates clusters of atoms near the critical size (Kirkpatrick, 1981) that would have otherwise grown into crystal nuclei upon decompression. Hence, because the pre-annealed samples did not produce anything that reasonably resembled the natural pumice crystal textures, we only interpret the results from experiments using natural untreated starting materials.

The use of powdered starting material, without prior fusion at super-liquidus conditions, means that the experiments contained crushed crystal fragments of all minerals in the phase assemblage (leucite, sanidine, pyroxene, etc.), in the proportions in which they existed prior to eruption. The melt is thus rich in heterogeneities, as is expected for a sub-liquidus magma. The IB–IT experiments were performed over ranges in temperature and pressure that bracket those that reproduce the major phenocryst and microphenocrysts phases found in the natural pumices (Fig. 1). About half of IB–IT experiments approached equilibrium crystallinity by melting and about half by crystallization. Coherence of textural results in runs from P–T conditions representing both lower and higher crystallinities than the starting material suggests that the direction of approach was not a factor controlling the final texture. Indeed, the effects of crushed leucite crystals from the pumices on any possible inherited experimental N_V should be random and invariant as a function of experimental pressure. Fig. 3 clearly shows that nucleation rate, calculated from measured experimental N_V, varies systematically with experimental pressure, and is thus not random, but depends on the experimental conditions. The same can be said about the variation of N_V with volume fraction (Fig. 5 b). This altogether supports that the experimental leucite N_V's are related to experimental conditions, and are not inherited from the starting powders.

The experimental leucites also exhibit euhedral and faceted shapes, consistent with interface-limited crystal growth textures (Kirkpatrick, 1981). Crushed leucites that had not undergone growth at experimental conditions would appear angular or even resorbed in the experiments. Thus, even if N_V was influenced by the distribution of crystals in the starting material, leucite growth proceeded as a function of the experimental conditions (Fig. 3).

In summary, the measured leucite N_V, sizes and habit in the IB–IT dataset all point towards internal consistency and not inherited textures from the pre-experimental sample material. Further comparisons between initially crystal-rich and crystal-free starting materials illustrate that leucites are likely to have formed in the presence of other phases. Thus, although we acknowledge that the crushed starting material probably helped to facilitate leucite formation through heterogeneous nucleation, the effects of inherited crystal number densities and growth rates directly from the un-annealed starting powders is relatively minor.

4.3. Thermal zoning within the upper reservoir

The IB–IT experiments indicate differences in magmatic temperatures between EU1 and EU2 in the reservoir. In EU1, euhedral, individual leucites crystallize homogeneously over almost the entire temperature range examined except at $T = 800$ °C. A minimum temperature between 800 °C and 825 °C can therefore be inferred. Also, amphibole, present in EU1 natural samples, cannot crystallize at $T > 860$ °C at ~100 MPa P_{H_2O} (Fig. 1) Thus, the EU1 magma likely had $T = 800–860$ °C. Amphibole stability offers a good marker in the 79 AD phonolites because it crystallizes at pressures greater than P_{H_2O} ~ 50 MPa, and is insensitive to volatile saturation conditions. The experiment which best reproduced the natural EU1 textures was run at $T = 840$ °C, and is a better match than experiments run at similar pressures at $T = 825$ °C and $T = 850$ °C. Hence, using this additional textural constraint, conditions for EU1 can be refined to $T = 830–840$ °C.

In the EU2 experiments, leucite textures comparable to the natural ones form only above 850 °C. Similarly, amphibole in EU2 is found to be stable experimentally at temperatures less than 875 to 925 °C. Thus, the EU2 magma was hotter, with $T = 850–925$ °C range. The experiment that best replicates the natural EU2 leucites is 79V1 ($T = 880$ °C). Hence, the Vesuvius 79 AD phonolite magmas were not only slightly compositionally zoned, but likely thermally layered as well. The thermal differences could arise from the late arrival of the K-tephritic melt batch which mixed deep within the chamber to form the grey tephriphonolitic magmas residing beneath the EU2 magma. In this configuration, temperatures are $T_{EU1} = 830–840$ °C, and $T_{EU2} = 850–925$ °C. These conditions are corroborated by Cioni et al. (1998), who found two distinct populations of homogenization temperatures in melt inclusions for the white magma: one between 800 and 850 °C, in agreement with EU1 temperatures found herein, and the other one between 900 and 950 °C, slightly higher than those derived for EU2.

4.4. Leucite crystallization conditions

In this study, phase equilibria data constrain leucite crystallization at $P_{H_2O} \approx 100$ MPa, and textural observations predict temperatures

$T=830$–840 °C for EU1 and $T=850$–925 °C for EU2. If magmas were H_2O-saturated in the Vesuvius 79 AD reservoir, then leucites might have grown under relatively steady, magma chamber-like conditions at ~4 km depth. On the other hand, if CO_2 was initially present in a deeper magma chamber (Scaillet and Pichavant, 2004; Iacono Marziano et al., 2007), leucites could have crystallized after slow depressurization or stalling during ascent. In this model, EU1 and EU2 magmas could originally have resided leucite-free at $P\geq200$ MPa. Slow depressurization (e.g. Scandone, 1996) could have begun at least several days before the Plinian phase of the eruption began, and gradually imposed a >100 MPa pressure drop in the reservoir. Once the leucite stability horizon was reached, the crystals grew to their final sizes in both EU1 and EU2 magmas, prior to ascent.

4.5. Leucite crystallization kinetics

4.5.1. Leucite nucleation

According to Fig. 3, experimentally-measured nucleation rates for leucites are dependent on ΔP, where $\Delta P=P_{\mathrm{reservoir}}-P_{\mathrm{nucleation}}$, and thereby on dissolved H_2O content and effective undercooling (T_{eff}). Crystal nucleation rates (I) depend on the energy necessary to form a cluster of critical size r*, which is generally termed the interfacial energy σ. In classical nucleation theory (CNT), I and σ are linked by the following equation (Kirkpatrick, 1981; Hammer, 2004):

$$I=\frac{A_c}{\eta}Texp\left(\frac{-\Delta G^*}{k_BT}\right) \quad (1)$$

where T is temperature, η is viscosity, k_B the Boltzmann constant, $A_c=\frac{k_Bn_V}{3\pi\lambda^3}$ is the pre-exponential factor with n_V volumetric concentration of reactant atoms and λ the jump distance between atoms, and $\Delta G^*=\frac{16\pi\sigma^3}{3\Delta G_V^2}S(\theta)$ is the free energy required to form critical nuclei having properties of the bulk solid, with θ the wetting angle between the nucleus-wall and nucleus-liquid interface. The bulk free energy change per volume during transformation $G_V=\frac{\Delta G}{V_M}$ encloses the volume of the crystallizing phase V_M as well as the energy change term, which can be approximated using Turnbull's equation $\Delta G=\frac{\Delta H\Delta T}{T_L}$, with T_L the liquidus temperature of the crystallizing phase at a given pressure, and ΔH is the enthalpy of formation of the phase from elements at T. Inserting the above equalities into Eq. (1) yields:

$$I=\frac{k_Bn_VT}{3\pi\lambda^3\eta}exp\left(\frac{-16\pi\sigma^3T_L^2V_M^2}{3\Delta H^2\Delta T^2k_BT}\right) \quad (2)$$

The interfacial energy can then be found by re-arranging Eq. (1) into:

$$\sigma=\left[\frac{\left[ln(I)-ln\left(\frac{k_Bn_VT}{3\pi\lambda^3\eta}\right)\right]\times3\Delta H^2\Delta T^2k_BT}{-16\pi T_L^2V_M^2}\right]^{\frac{1}{3}} \quad (3)$$

In these calculations, several assumptions are made, such as $S(\theta)=1$ (homogeneous nucleation), a compositional dependence of the interfacial energy, and the use of T_{eff} instead of ΔT (Hammer, 2004). ΔH and V_M vary with P and T, ranging from $\Delta H=175{,}902$ to $193{,}686$ J K^{-1} and $V_M=8.93$ to 8.94×10^{-5} m^3 mol^{-1} (taken from the Computational Thermodynamics Server: http://ctserver.ofm-research.org/phaseProp.html; see references therein), a jump distance $\lambda=3\times10^{-10}$ m was used (Hammer, 2004), T_{eff} and T_L were measured using phase curves from Fig. 1, and viscosities were calculated following the models of Shaw (1972) and Romano et al. (2003). Nucleation rates (I) were input in two different ways:

First, and because nucleation rate seems to be mostly P-dependent (Fig. 3), a logarithmic best fit function applied to all experiments was inserted into Eq. (3)

$$I=-1.9325\times10^8\ln(\mathrm{P})+9.42\times10^8 \quad (4)$$

Because H_2O content directly depends on P, the equation can also be written:

$$I=-3.646\times10^8\ln(\mathrm{H_2O})+5.536\times10^8 \quad (5)$$

σ was then calculated using Eq. (3) for different temperatures (800, 825, 850 and 875 °C) over the pressure range covered by the experiments (25–125 MPa). We emphasize that the calculated interfacial energy includes effects not accounted for by the CNT which reduce the nucleation barrier, and adopt σ' instead of σ (Hammer, 2004).

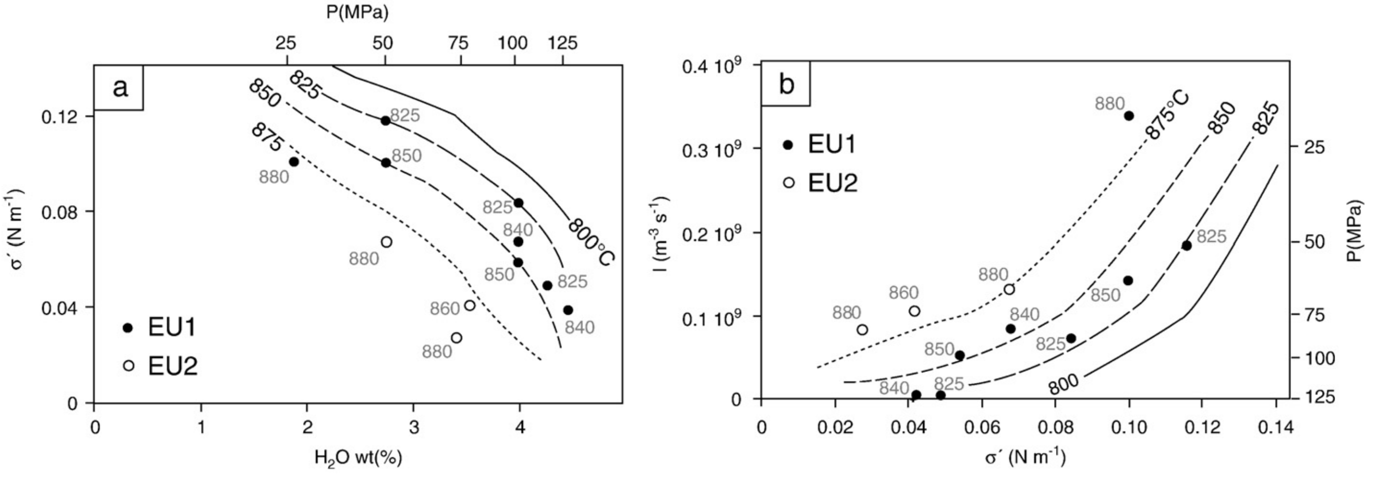

Fig. 6. Link between interfacial energy σ', nucleation rates I, and intensive variables such as pressure (and thereby water content). Isotherm curves show calculated σ' in EU1 for four temperatures using Eq. (3) in the text. Note that they are *not* best-fitting curves for the individual experimental runs (temperatures displayed in grey). (a) Interfacial energy decreases with increasing water content and (b) nucleation rate (and thereby pressure) increases with σ'.

Secondly, in an attempt to compare the interfacial energy calculated using the term *I* derived from Eqs. (4) and (5), with interfacial energy calculated using nucleation rates measured in each individual run (Table 3), each experiment was plotted, along with its run conditions. Because leucite nucleation rates are pressure-dependent, co-variations between σ', *P*, H_2O, and *I* are expected.

Fig. 6 illustrates the results obtained for the present experiments, in terms of interfacial energy, viscosity, and nucleation rate. As in Hammer (2004), σ' decreases with increasing experimental H_2O pressure, suggesting a compositional control on nucleation kinetics (Fig. 6a). Hence, at the inferred T conditions for EU1 and EU2 and for pressures $P \sim 100$ MPa, surface tension is roughly $\sigma' \approx 0.07\ \mathrm{N\ m^{-1}}$ for EU1 and $\sigma' \leq 0.05\ \mathrm{N\ m^{-1}}$ for EU2. Nucleation rates (*I*) show a positive correlation with increasing interfacial energy (Fig. 6b). This is expected from Eq. (3) since interfacial energy is related to the logarithm of nucleation rate by a cubic root. The slight temperature-dependence of σ' illustrates that the interfacial energy decreases as *T* increases (Fig. 6a and b). A temperature-dependence of nucleation rate is also observed when $T_{\text{eff.}}$ with is confronted to I (see Fig. A3 in the additional material). Because viscosity decreases with increasing H_2O content at fixed temperature, and since changes in dissolved H_2O strongly affect melt viscosity, the interfacial energy scales with viscosity.

Measured nucleation rates (*I*) and calculated viscosities (η) support that nucleation rate increases as melt viscosity increases (additional material, Fig. A3). A theoretical basis for this trend may not be obvious, since nucleation rate is inversely related to melt viscosity in Eq. (2). However, the main control on nucleation rate in Eq. (2) is the cubed interfacial energy term, which is in turn controlled by dissolved water content. Hence, the kinetic limitation imposed by increasing viscosity exerts a weaker control in leucite nucleation than surface tension, although both are intrinsically linked to water content.

A complex interplay between nucleation and growth produces the observed natural and experimental textures. The viscosity increase accompanying melt devolatilization inhibits diffusion of crystal-forming components, and this may enhance nucleation over the growth of preexisting crystals. This hypothesis is supported by the correlation of leucite volume fraction and N_V (Fig. 5b), and lack of correlation between volume fraction and mean size. These trends suggest leucite crystallization is accomplished through vigorous nucleation (followed by growth) rather than by rapid growth of sparse crystals. Note that in Fig. 6a and b, individual experiments are reasonably well modeled by the calculated isotherms, indicating internal consistency of the dataset and demonstrating a viability of our application of the classical theory of nucleation.

While the relationship between pressure and nucleation rate is clear over the examined P range, the same is not obvious for temperature (additional material, Fig. A2). Indeed, viscosity in these melts is much more influenced by P_{H2O} than by T in the studied range (also see Fig. A3). The limited dataset suggests that variations in nucleation rate as a function of P_{H2O} are larger than those caused by variations in T.

4.5.2. Mechanisms of leucite formation

In contrast to the clear relationship between leucite number density and pressure, the correlation between leucite size and P is less obvious. Size appears to be mostly affected by pressure at values over 100 MPa, close to the phase stability limit (i.e., growth rates on Fig. 3). In contrast, temperature does not affect leucite size within a large P–T domain, but produces changes in leucite shape and arrangement, particularly at T below 825 °C in EU1 and below 850 °C in EU2, below which leucites become increasingly clustered.

Based on the textural observations, and the relationships between nucleation and growth rates with varying P and T, we derive a model for leucite growth mechanisms in EU1 and EU2 phonolitic melts (Fig. 7). At the vicinity of the leucite stability curve, growth rates are much higher than at lower pressures (Fig. 3). Growth-dominant behavior is expected at low degrees of supersaturation where nucleation rates are low and nutrient transport to a few nuclei is rapid (Kirkpatrick, 1981). This tendency is also observed in the experiments of Hammer and Rutherford (2002): plagioclase phenocrysts grow immediately upon decompression, while nucleation of new crystals (destined to become microlites) occurs at higher undercoolings. Near the stability curve, the experimental leucites possess sharp, faceted interfaces (Fig. 2e) and their habit is typically euhedral. Further away from the stability limit, nucleation rate increases and growth continues at a relatively high rate, producing crystallization of numerous euhedral leucites which grow to an average size of ~19 and 25 μm for EU2 and EU1 respectively. Within the "growth" and "nucleation + growth" domains, diffusion of nutrients is uninhibited by melt viscosity and growth may be interface-limited. Indeed, faceted crystal morphologies suggest that growth rate is limited by attachment of atoms and not by transport of nutrients in the melt. With increasing distance from the leucite-in curve, the "nucleation + growth" regime is replaced by the "nucleation dominated" domain in which crystals form as aggregates (Fig. 2f) or massive intergrowths very similar to those observed in the SSD experiments. Here, diffusion of nutrients to the melt-crystal interface is most likely a limiting process, and the system responds to thermodynamic disequilibrium by vigorous nucleation. The trend is similar for EU2 compositions, except that temperatures defining the regimes are shifted upward (Fig. 7).

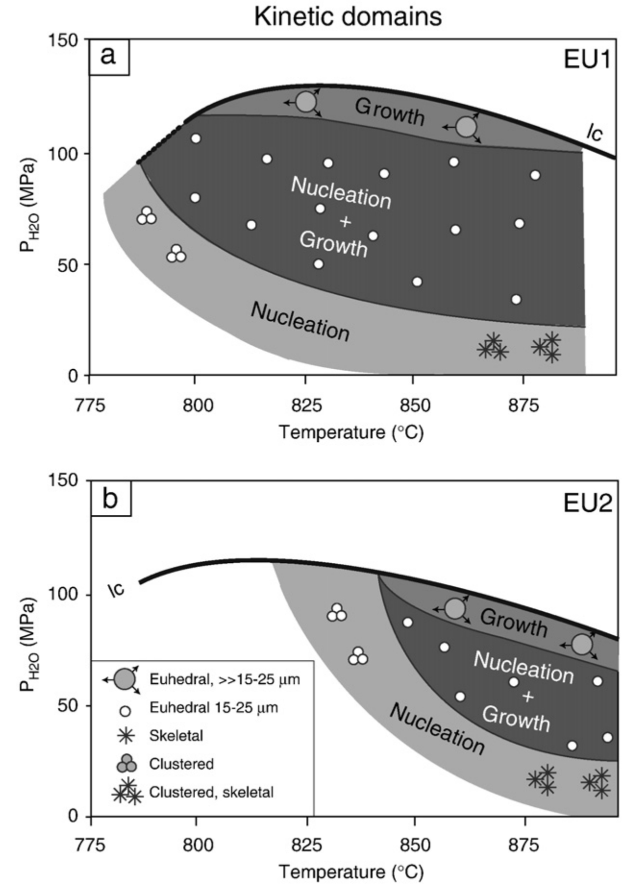

Fig. 7. Interpretative diagrams of crystallization kinetics for (a) EU1 and (b) EU2 leucites. Three mainly pressure-dependent regimes are represented, growth, nucleation + growth and nucleation-dominated domains. Symbols are generic and do not represent specific experiments.

4.5.3. Comparisons with plagioclase crystallization kinetics

Interesting comparisons can be made between crystallization kinetics of leucites and plagioclase in magmas of various compositions.

The time-averaged leucite growth rates constrained from the present experiments vary between 2×10^{-8} mm s^{-1} and ~10^{-7} mm s^{-1}. In comparison, growth rates calculated from CSD for plagioclase phenocrysts vary between 10^{-8} mm s^{-1} and 10^{-11} mm s^{-1} (Cashman, 1988; Cashman and Blundy, 2000; Armienti et al., 2007), and between 10^{-7} and 10^{-10} mm s^{-1} for microlites (Cashman, 1988). Thus, leucites have growth rates that are 1 to 3 orders of magnitude faster than those calculated for plagioclase. Hammer and Rutherford (2002), Couch et al. (2003), and Larsen (2005) have nevertheless demonstrated that growth rates are extremely variable as a function of experimental duration, decreasing precipitously as runtime increases, which is consistent with crystallization kinetics being slower as the system approaches thermodynamic equilibrium. Because growth rates for leucites from this study have been obtained at presumably low degrees of effective undercooling, comparisons must be made with plagioclase under similar conditions. Using asymptotes of the time-variation of plagioclase growth rate obtained from Hammer and Rutherford (2002) for dacites, and Larsen (2005) for rhyodacites, at low undercooling ($T_{eff}=34$–35 °C), growth rates are 2×10^{-9} mm s^{-1} and 3×10^{-9} mm s^{-1} respectively. Differences between plagioclase and leucites could be, to a first order, attributed to viscosity differences; indeed, at similar P–T conditions, phonolites have significantly lower viscosities than dacites (see Fig. A3 in additional material) and rapid diffusion may allow for faster growth in phonolites. Even so, plagioclase growth rates estimated using CSD's from low viscosity basaltic melts (Armienti et al., 2007) are of the same magnitude as those obtained experimentally by Hammer and Rutherford (2002) in dacites after sufficiently long runtimes. Altogether, this suggests that leucites in phonolitic melts grow faster than plagioclase in other melts for reasons that cannot be attributed solely to viscosity.

Leucite nucleation rates of 0.0007 to 0.34 mm^{-3} s^{-1} from the experiments encompass those measured by Cashman and Blundy (2000) for plagioclase microphenocrysts, but are much higher than estimated for plagioclase phenocrysts, estimated to be 5–21×10^{-9} mm^{-3} s^{-1} in a Mt St Helens dacite (Cashman, 1988). On the other hand, leucite nucleation rates are much lower than the 2 to 10,000 mm^{-3} s^{-1} range observed for plagioclase microlites by Larsen (2005), and at the lower end of the 0.01–4 mm^{-3} s^{-1} interval found by Hammer and Rutherford (2002).

In terms of crystallization dynamics, low nucleation rates for leucite or plagioclase microphenocrysts (0.007–0.34 mm^{-3} s^{-1}) suggest nucleation triggered by changes in ΔT_{eff} that are slow enough for the system to respond to the thermodynamic disturbances. In contrast, the much higher plagioclase microlite nucleation rates (2–10,000 mm^{-3} s^{-1}) support a nucleation-dominant regime during rapid changes in P–T conditions, in which diffusion of crystal-forming components in the melt is rate-limiting (for additional details regarding leucite and plagioclase nucleation behavior, see also Fig. A4 and related text in the additional material).

4.5.4. Leucite size-invariance

In the above paragraphs, it appears that the observed leucite crystallization generally conforms to classical theory of nucleation and growth. At high and low undercoolings, nucleation and growth of leucites behave similarly to plagioclase, albeit at different rates (Hammer and Rutherford, 2002; Couch et al., 2003). At intermediate undercoolings, however, leucite in phonolitic melts behaves in a more complex fashion. While nucleation rates continuously increase with increasing effective undercooling, growth rates appear to decrease rapidly away from the stability curve and remain constant throughout a large P and T domain (Fig. 3). In this domain, leucites seem to reach a consistent size-distribution even as volume fraction varies significantly. Interestingly, the size attained within these conditions is larger for EU1 than for EU2 (~25 μm and ~19 μm respectively). This raises two questions: why would crystals stop growing after reaching a certain size? And why would these sizes be different in the two phonolites?

One possibility is that growth rate decreases as crystals coarsen. The final size distribution may be achieved by fast growth rates shortly after the system is thermodynamically perturbed. As chemical and thermodynamic equilibrium is approached, growth rate declines precipitously as has been observed for plagioclase and other phases forming in response to decompression (Hammer and Rutherford, 2002; Couch et al., 2003), thus preserving the size distribution that was set by the initial growth rate. A time-series of experiments is needed to test whether this is a viable explanation.

Ostwald ripening may also be important in achieving this textural invariance. Polydisperse mixtures in chemical equilibrium with melt are not at their lowest energy state due to non-zero interfacial energy expended at crystal surfaces (Voorhees, 1992). Full textural and thermodynamic equilibrium can only be achieved through a reduction in interfacial energy. During Ostwald ripening, the total crystal-melt interfacial energy is reduced through diffusion of crystalline nutrients from zones of high interfacial curvature to zones of low interfacial curvature. Accordingly, small crystals are lost to feed larger ones until the system reaches a “textural steady-state”. Although not entirely conclusive, leucite distribution curves for both natural and experimental samples (Fig. 5a) indicate this type of coarsening. However, the rate at which these processes occur is uncertain. While Park and Hanson (1999) showed that Ostwald ripening can initiate substantial textural modifications, experiments on olivine-bearing basalts and plagioclase-bearing andesites by Cabane et al. (2005) revealed that this process is only significant for one of the studied crystal phases (olivine) in one of the studied compositions (basalt). Much more work is needed to substantiate the influence of ripening processes on modifying crystal populations in volcanic rocks.

Finally, the shift in size distributions observed between EU1 and EU2 might result from small chemical variations in K_2O, Na_2O, Al_2O_3, and SiO2 between the two magmas (Table 1). In this scenario, leucites reach ~18 μm in EU2 after 5 days compared to 25 μm in EU1. It is nonetheless hard to demonstrate how such small variations in chemistry could induce large differences in the formation of crystalline phases in magmas.

5. Conclusions

In the 79 AD magmas, leucite microphenocrysts did not crystallize during rapid magma ascent at average rates typical of Plinian eruptions. Rather, they are likely to have grown over timescales of days at lower, more slowly imposed effective undercoolings. The study of leucite crystallization yielded not only a minimum timing for magma residence at depth, but also provided two possible scenarios yielding strong clues to magma storage and pre-eruptive dynamics occurring under volcanoes such as Vesuvius. In the first scenario, if the white magma was water-saturated, magma was stored for at least a few days at depths of ~4 km before being erupted. Alternatively, if the magma was undersaturated, leucites may have captured a slow depressurization event at greater depth prior to entering the conduit. Furthermore, at similar temperatures, EU1 and EU2 displayed different crystallization behaviors, yielding a remarkable example of how minor chemical divergences may have a measurable effect on crystallization kinetics. Although leucite crystallization is well described by the classical nucleation theory, a small complication not described by classical formulation was observed: a characteristic textural state appears to be attained over a rather large P–T domain, with invariant sizes but variable population number densities. Finally, the leucite growth and nucleation rates derived from these experiments may be used in the future as proxies to assess magma residence times or rise times in the event of eruptions involving slower ascent.

Acknowledgments

The authors wish to acknowledge NSF grants EAR 0537950 and 0537543. Kathy Cashman's input enriched this work, and comments from Bruno Scaillet, Michelle Coombs and Jon Blundy improved a previous version of the manuscript. Roberto Scandone's comments were also appreciated.

Appendix A. Supplementary data

Supplementary data associated with this article can be found, in the online version, at doi:10.1016/j.epsl.2009.02.014.

References

Armienti, P., Francalanci, L., Landi, P., 2007. Textural effects of steady-state behavior of the Stromboli feeding system. J. Volcanol. Geotherm. Res. 160, 86–98.

Barberi, F., Bizouard, B., Clocchiatti, R., Metrich, N., Santacroce, R., Sbrana, A., 1981. The Somma–Vesuvius chamber: a petrological and volcanological approach. Bull. Volcanol. 44, 295–315.

Cabane, H., Laporte, D., Provost, A., 2005. An experimental study of Ostwald ripening of olivine and plagioclase in silicate melts: implications for the growth and size of crystals in magmas. Contrib. Mineral. Petrol. 150, 37–53.

Carey, S., Sigurdsson, H., 1987. Temporal variations in column height and magma discharge rate during the 79 A.D. eruption of Vesuvius. Geol. Soc. Am. Bull. 99, 303–314.

Cashman, K.V., 1988. Crystallization of Mount St Helens 1980–1986 dacite: a quantitative textural approach. Bull. Volcanol. 50, 194–209.

Cashman, K., 1992. Groundmass crystallization of Mount St Helens dacites, 1980–1986: a tool for interpreting shallow magmatic processes. Contrib. Mineral. Petrol. 109, 431–449.

Cashman, K., Blundy, J., 2000. Degassing and crystallization of ascending andesite and dacite. Philos. Trans. – Math. Phys. Eng. Sci. 358 (1770), 1487–1513.

Cioni, R., 2000. Volatile content and degassing processes in the 79 AD magma chamber at Vesuvius (Italy). Contrib. Mineral. Petrol. 140, 40–54.

Cioni, R., Marianelli, P., Sbrana, A., 1992. Dynamics of the AD 79 eruption: stratigraphic, sedimentological and geochemical data on the successions from the Somma–Vesuvius southern and eastern sectors. Acta Vulcanol. 2, 109–123.

Cioni, R., Civetta, L., Marianelli, P., Metrich, N., Santacroce, R., Sbrana, A., 1995. Compositional layering and syn-eruptive mixing of periodically refilled shallow magma chamber: the A.D. 79 Plinian eruption of Vesuvius. J. Pet. 36, 739–776.

Cioni, R., Marianelli, P., Santacroce, R., 1998. Thermal and compositional evolution of the shallow magma chamber of Vesuvius: evidence from pyroxene phenocrysts and melt inclusions. J. Geophys. Res. 103 (B8), 18277–18294.

Couch, S., Sparks, R.S.J., Carroll, M.R., 2003. The kinetics of degassing-induced crystallization at Soufriere Hills, Montserrat. J. Pet. 44, 1477–1502.

Gardner, J.E, Hilton, M., Carroll, M.R., 1999. Experimental constraints on degassing of magma: isothermal bubble growth during continuous decompression from high pressure. Earth Planet. Sci. Lett. 168, 201–218.

Gardner, J.E, Hilton, M., Carroll, M.R., 2000. Bubble growth in highly viscous silicate melts during continuous decompression from high pressure. Geochim. Cosmochim. Acta. 64, 1473–1483.

Geshwind, C., Rutherford, M.J., 1995. Crystallization of microlites during magma ascent: the fluid mechanics of recent eruptions at Mount St. Helens. Bull. Volcanol. 57, 356–370.

Gurioli, L., Houghton, B.F., Cashman, K.V., Cioni, R., 2005. Complex changes in eruption dynamics during the 79 AD eruption of Vesuvius. Bull. Volcanol. 67, 144–159.

Hammer, J.E., 2004. Experimental nucleation data applied to classical theory. Am. Mineral. 89, 1673–1679.

Hammer, J.E., Rutherford, M.J., 2002. An experimental study of the kinetics of decompression-induced crystallization in silicic melt. J. Geophys. Res. 107 (B1), 1–24.

Hess, K.-U., Dingwell, D.B., 1996. Viscosities of hydrous leucogranitic melts: a non-Arrhenian model. Am. Mineral. 81, 1297–1300.

Iacono Marziano, G., Schmidt, B.C., Dolfi, D., 2007. Equilibrium and disequilibrium degassing of a phonolitic melt (Vesuvius AD 79 “white pumice”) simulated by decompression experiments. J. Volcanol. Geotherm. Res. 161, 151–164.

Kirkpatrick, T.J., 1981. Kinetics of crystallization of igneous rocks. Rev. Mineral. 8, 321–398.

Larsen, J.F., 2005. Experimental study of plagioclase rim growth around anorthite seed crystals in rhyodacite. Am. Mineral. 90, 417–427.

Larsen, J.F., 2008, Heterogeneous bubble nucleation and disequilibrium H_2O exsolution in Vesuvius K-phonolite melts. J. Volcanol. Geotherm. Res. 275, 278–288.

Lirer, L., Pescatore, T., Booth, B., Walker, G.P.L., 1973. Two Plinian pumice-fall deposits from Somma–Vesuvius, Italy. Geol. Soc. Am. Bull. 84, 759–772.

Mastin, L.G., 2002. Insights into volcanic conduit flow from an open-source numerical model. Geochem. Geophys. Geosyst. 3, 7.

Papale, P., Dobran, F., 1993. Modeling of the ascent of magma during the Plinian eruption of Vesuvius in A.D. 79. J. Volcanol. Geotherm. Res. 58, 101–132.

Park, Y., Hanson, B., 1999. Experimental investigation of Ostwald-ripening of forsterite in the haplobasaltic system. J. Volcanol. Geotherm. Res. 90, 103–113.

Romano, C., Giordano, D., Papale, P., Mincione, V., Dingwell, D.B., Rosi, M., 2003. The dry and hydrous viscosity of alkaline melts from Vesuvius and Phlegrean Fields. Chem. Geol. 202, 23–38.

Rutherford, M.J., 1996. Conditions in the pre-eruption 79 AD Vesuvius magmas: controls on magmatic and eruption processes. Vesuvius Decade Volcano, Workshop Handbook, IAVCEI-CEV, IAVCEI-CMVD, 17–22 September 1996.

Rutherford, M.J., Gardner, J.E., 2000. Rates of Magma Ascent. In: Sigurdsson, H. (Ed.), Encyclopedia of Volcanoes. Academic Press, pp. 207–218.

Sahagian, D.L., Proussevitch, A.A., 1998. 3D particle size distributions from 2D observations: stereology for natural applications. J. Volcanol. Geotherm. Res. 84, 173–196.

Scaillet, B., Pichavant, M., 2004. Crystallisation conditions of Vesuvius phonolites. Geophys. Res. Abstr. 6, 03764.

Scandone, R., 1996. Factors controlling the temporal evolution of explosive eruptions. J. Volcanol. Geotherm. Res. 72, 71–93.

Shaw, H.R., 1972. Viscosities of magmatic silicate liquids: an empirical method of prediction. Am. J. Sci. 272, 870–893.

Sheridan, M.F., Barberi, F., Rosi, M., Santacroce, R., 1981. A model for Plinian eruptions of Vesuvius. Nature 289, 282–285.

Sigurdsson, H., Carey, S., Cornell, W., Pescatore, T., 1985. The eruption of Vesuvius in A.D. 79. Natl. Geog. Res. 1, 332–387.

Voorhees, P.W., 1992. Ostwald ripening of two-phase mixtures. Annu. Rev. Mater. Sci. 22, 197–215.